



# Maximising *E*-waste leachate adsorption: multi-component isotherm models and mechanisms with scalable mesoporous sugarcane bagasse-derived biochar

Amthal Al-Gailani<sup>a,\*</sup>, Julius G. Bongosia<sup>a</sup>, Karl Hornsby<sup>b</sup>, Martin J. Taylor<sup>a</sup>

<sup>a</sup> School of Engineering and Technology, Chemical Engineering, University of Hull, Hull HU6 7RX, United Kingdom

<sup>b</sup> School of Natural Science, Chemistry, University of Hull, Hull HU6 7RX, United Kingdom

## ARTICLE INFO

Editor: Ludovic F. Dumée

### Keywords:

Sugarcane bagasse biochar  
Mesoporous adsorbents  
Multi-component isotherm modelling  
Adsorption mechanism  
*E*-waste

## ABSTRACT

Heavy metal contamination is a primary environmental and health concern contributing to organ damage, neurological disorders and developmental issues. Adsorption is an efficient, cost-effective method for removing heavy metals from contaminated water. In this study, the adsorption of five metals ( $\text{Cu}^{2+}$ ,  $\text{Ni}^{2+}$ ,  $\text{Pb}^{2+}$ ,  $\text{Ag}^+$  and  $\text{Mn}^{2+}$ ) into mesoporous sugarcane bagasse-derived biochar (surface area:  $1061.77 \text{ m}^2 \text{ g}^{-1}$ ) was investigated using multi-component isotherm models, including Extended Langmuir (EL), Extended Freundlich (EF), Modified Competitive Langmuir (MCL) and Extended Sips (ES). The biochar was synthesised via KOH activation (1, 1 w/w) followed by pyrolysis at  $800 \text{ }^\circ\text{C}$ . The ES model was found to best describe the competitive adsorption behaviour. Among the tested metals,  $\text{Pb}^{2+}$  exhibited the highest adsorption capacity ( $605.45 \text{ mg/g}$ ), followed by  $\text{Cu}^{2+}$  ( $501.77 \text{ mg/g}$ ). Kinetic analysis using pseudo-first-order and pseudo-second-order models confirmed chemisorption superiority, specifically for  $\text{Cu}^{2+}$ ,  $\text{Mn}^{2+}$ , and  $\text{Pb}^{2+}$ . The rate-limiting step was temperature-dependent; intraparticle diffusion dominated at  $25 \text{ }^\circ\text{C}$ , while chemisorption prevailed at  $55 \text{ }^\circ\text{C}$ . The thermodynamic analysis ( $\Delta H > 0$ ,  $\Delta G < 0$ ) confirmed that the adsorption process is endothermic and spontaneous under the tested conditions. After three regeneration cycles, the biochar structure stability is confirmed with evidence of full adsorbate removal.

## 1. Introduction

Heavy metal pollution in water supplies has reached a crisis level, sullying drinking water and limiting sources of clean water for developed and developing nations, preventing the realisation of the United Nation's Sustainable Development Goal 6 – Clean Water and Sanitation. A long-term study over 45 years concluded that the average concentration of 12 heavy metals in rivers and lakes around the globe, has increased. Many of these sites have developed from single metal contamination into areas with rich mixtures of varying heavy metals such as; copper, nickel, manganese and lead [1]. This increase in metal concentration has introduced wider health risks among humans, especially through the ingestion of heavy metals due to proximity and exposure to contaminated bodies of water. The ingestion of heavy metals via the oral route is a common pathway of exposure. Elevated concentrations of these metals can severely impact multiple organ systems, leading to neurological impairments, respiratory complications,

carcinogenic effects, gastrointestinal obstruction, and osteoporosis [2,3]. Research indicates that children are more vulnerable to these health risks than adults, with 21.6 % of non-carcinogenic risks and 53.2 % of carcinogenic risks exceeding the recommended safety thresholds [4]. Lead exposure constitutes a substantial public health burden. According to estimates from the Institute for Health Metrics and Evaluation (IHME), lead exposure was responsible for over 1.5 million deaths worldwide in 2021, predominantly due to its cardiovascular effects [5]. The IHME also reported that nickel exposure caused 9850 deaths globally in 2021 [6]. Furthermore, approximately one in three children worldwide (~800 million) have blood lead levels of  $\geq 5 \text{ } \mu\text{g/dL}$ , a concentration at which medical intervention is advised as it is linked with high blood pressure as well as damaging the brain and kidneys [7].

One key problem with addressing metal contamination in humans is its resistance to decomposition, making digestion harder. Thus, it accumulates and stays in the body of a living organism for extended periods, a phenomenon known as bioaccumulation [2]. This contributes to

\* Corresponding author.

*E-mail address:* [A.Z.Al-Gailani@hull.ac.uk](mailto:A.Z.Al-Gailani@hull.ac.uk) (A. Al-Gailani).

<https://doi.org/10.1016/j.jwpe.2025.107979>

Received 20 March 2025; Received in revised form 11 May 2025; Accepted 18 May 2025

Available online 20 May 2025

2214-7144/© 2025 The Authors. Published by Elsevier Ltd. This is an open access article under the CC BY license (<http://creativecommons.org/licenses/by/4.0/>).

the biomagnification of heavy metals, where the concentration of contaminants increases as they travel up the food chain through consumption of food contaminated by heavy metals [8]. As a result, addressing the presence of specific metals based in contaminated water systems rather than widespread remediation is paramount.

Another contributing factor to heavy metal contamination in water is the global proliferation of Waste Electrical and Electronics Equipment (WEEE), colloquially known as e-waste. According to the World Health Organization (WHO), in 2022, 62 million metric tonnes of e-waste were generated. Of these, only 22.3 % were recycled [9]. It is predicted that by 2030, global e-waste production will reach 74 million metric tonnes [10]. Household electrical appliances, especially personal computers (PCs) and mobile phones, contribute to approximately 50 % of the overall e-waste production [11]. The decay and degradation of organic waste, combined with general household waste, creates an acidic or basic environment, depending on the type of waste referred to as a leachate. This process digests metals in the e-waste into an aqueous phase, this will then percolate through the ground and contaminate groundwater, with rainwater often facilitating the transfer of metals. Through infiltration and transport systems, metal-contaminated water can reach tributaries or areas of land use [12]. Leachable metals include Cu, Cd, Cr, Mn, Ni, Co, Ta, W, Nd, Pb and Al. For instance, the Pb content in Random Access Memory (RAM) and the Central Processing Unit (CPU) is around 57 and 27 g/dry kg, respectively, while Integrated Drive Electronics cables contain approximately 4.4 g/dry kg of Cu and 10 g/dry kg of Ni [13].

Despite the severity of the issue, researchers have explored a variety of strategies to mitigate heavy metal contamination [14,15]. One such solution is biochar, a sustainable, net-zero adsorbent produced from second generation lignocellulosic feedstocks such as rice husk [16,17], sugarcane bagasse [18], corn straw [19], food waste [20], and leaves [21,22]. Biochar offers a low-cost way to uptake heavy metals from water while also being an avenue to reuse organic waste materials that would otherwise be disposed of. Biochar is able to separate aqueous-metal suspensions through a combination of mechanisms like electrostatic interactions, pore filling,  $\pi$ -electron donor-acceptor interactions, hydrophilicity and hydrogen bonding, as well as physical interactions such as precipitation [23,24].

The modelling of this process is important for understanding the mechanisms governing adsorption, optimising operating conditions and predicting the performance of adsorbents in real-world scenarios [25]. Adsorption isotherm models, particularly multi-component models, play a key role in evaluating the capacity and efficiency of adsorbents in removing multiple metal ions simultaneously, offering insights into the interactions between adsorbate and adsorbent surfaces, pore size/volume and available surface area.

While conventional single-component adsorption models such as the Langmuir or Freundlich isotherms simplify system behaviour, they do not account for the complex competitive interactions that occur in multi-metal systems [26]. Multi-component adsorption modelling offers a realistic, and comprehensive approach to heavy metal removal compared to single-component models. Multi-component models, such as the Extended Langmuir, Extended Langmuir–Freundlich, Modified Competitive Langmuir, and Extended Sips incorporate interaction coefficients, heterogeneity indices and mole fraction parameters to simulate these dynamics. This enables accurate predictions of adsorption behaviour in binary or multi-component systems. Between 1986 and 2023, only 1.9 % (401 out of 20,894) of scientific articles on adsorption focused on multi-component modelling. Most of these studies investigated binary systems due to the higher complexity involved in modelling systems with more components [25].

This work involves modelling the adsorption of five main block metals, Cu, Ni, Pb, Ag, and Mn, from a single aqueous solution, using a sugarcane bagasse-derived biochar with defined pore structure and expansive surface area, under optimised batch conditions, as deduced in our previous work [18]. This study selected these metals because of their

**Table 1**

Textural and chemical properties of the optimised mesoporous bagasse biochar.

$m_{\text{KOH}}/$ $m_{\text{SCB}}$	C (wt %)	H (wt %)	N (wt %)	Ash (wt %)	BET Surface Area ( $\text{m}^2 \text{g}^{-1}$ )	Pore volume ( $\text{cm}^3$ $\text{g}^{-1}$ )	Average pore diameter (nm)
1.00	44.60	2.43	0.24	24.56	1061.77	0.33	5.70

high concentrations in e-waste leachate and their significant toxic effects [11,12]. Multi-component models, namely Extended Langmuir, Extended Langmuir–Freundlich, Modified Competitive Langmuir and Extended Sips, were employed for the adsorption isotherms. Regarding the adsorption kinetics, the experimental data were fitted to pseudo-first-order (PFO) and pseudo-second-order (PSO) models. Moreover, the rate-limiting step that control the adsorption process was determined by adopting a recently proposed multi-mechanism kinetic model. Finally, the thermodynamic feasibility of the multi-component adsorption process was determined. Together, these modelling efforts aim to improve the understanding of multi-metal adsorption and aid in designing more effective water treatment systems.

## 2. Methods

### 2.1. Experimental procedure

Optimised mesoporous sugarcane bagasse-derived biochar was produced and activated using the method shown in our previous work [27]. Specifically, biochar was created through the 1:1 ratio of leached bagasse and KOH and pyrolysed at 800 °C before digesting the K residues in 5 M HCl, generating an effective adsorbent with textural and chemical properties summarised in Table 1. Materials were characterised as follows; data pertaining to the parent sugarcane bagasse feedstock can be found in prior work [18]. Ultimate analysis (CHN) of the biochar was acquired using a LECO CHN628 analyser. Ash content was determined using a Mettler Toledo TGA/DSC 1 in air at 30 mL/min, with a ramp rate of 10 °C/min from room temperature to 750 °C, holding for 1 h. The morphology and size of biochar grains were examined using a Zeiss EVO 60 Scanning Electron Microscope (SEM) at  $10^{-2}$  Pa and an electron acceleration voltage of 20 kV. For high-contrast imaging, the sample was coated with Au. Fig. 1 shows SEM images of the mesoporous sugarcane bagasse-derived biochar at increasing magnification. The surface area and pore volume/size of the biochar were analysed at  $-196$  °C using a Micromeritics TriStar porosimeter, prior to analysis the sample was degassed for 3 h at 110 °C under a nitrogen capillary feed.

Batch, multi-metal uptake trials were conducted under parallel conditions using a Radley's Starfish reactor platform to ensure identical mixing and thermal stability across the trials. Each reactor flask was charged with 5 mg of the optimised biochar in a 100 mL reaction solution containing varied metal concentrations of Cu (copper sulfate pentahydrate, Honeywell, 98 %) [5–35 ppm], Ni (Nickel (II) nitrate hexahydrate, ThermoFisher Scientific, 98 %) [5–35 ppm], Mn (Manganese (II) nitrate tetrahydrate, Sigma-Aldrich,  $\geq 97$  %) [5–35 ppm], Pb (Lead (II) chloride, ThermoFisher Scientific, 99 %) [2.5–20 ppm] and Ag (Silver nitrate, ThermoFisher Scientific,  $\geq 99$  %) [2.5–20 ppm]. Each reactor was operated at 25 °C, at atmospheric pressure, stirring at 300 rpm and configured to pH 10. These conditions were previously found to be the optimum conditions for the biochar to maximise Cu (II) removal [18]. Aliquots were removed (2 mL) from each batch reactor temporally across 0, 2, 5, 8, 13, 20, and 30 mins and diluted to a total volume of 10 mL. Diluted samples were then analysed via Inductively Coupled Plasma Optical Emission Spectroscopy (ICP-OES) (iCAP 7400 Radial, Thermo Scientific) without any additional digestion. All experiments were performed in triplicate to ensure the consistency and reproducibility of the data.

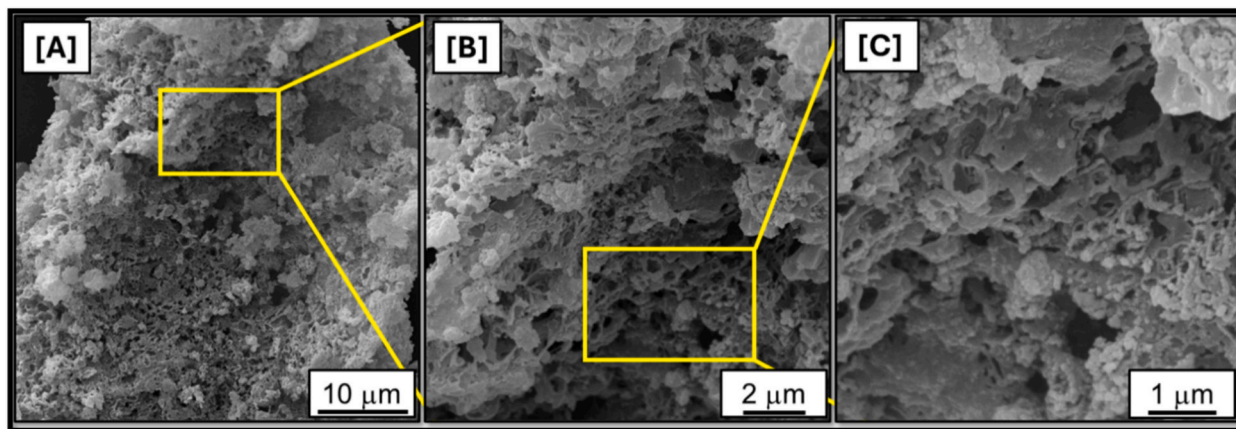


Fig. 1. SEM images at increasing magnification of 1.00 mKOH/mSCB mesoporous biochar.

The regeneration and reusability of the biochar were evaluated through a series of three adsorption–desorption cycles. A mixed-metal solution was prepared containing  $\text{Cu}^{2+}$ ,  $\text{Ni}^{2+}$ , and  $\text{Mn}^{2+}$  at 15 ppm each, and  $\text{Pb}^{2+}$  and  $\text{Ag}^+$  at 10 ppm each. A total of 210 mg of the optimised biochar was added to the solution, and the pH was adjusted to 10 using 0.2 M HCl or 0.2 M NaOH. The suspension was stirred at 300 rpm for 0.5 h at 20 °C to ensure equilibrium.

After adsorption, the biochar was recovered by centrifugation (Thermo Fisher Sorvell ST16 centrifuge, 6000 rpm for 0.25 h) followed by refluxing in 200 mL of 5 M HCl for 0.5 h to digest adsorbed metals. The biochar was then filtered and washed thoroughly with deionised water until the washings became colourless. A portion of the regenerated biochar was dried overnight (Fisherbrand gravity convection at 105 °C) and taken for XRD analysis. A Powder X-ray diffraction (PXRD) with monochromated Cu  $K\alpha$  radiation ( $\lambda = 0.1542$  nm) on a PANalytical Empyrean series 2 diffractometer was used, sample mounting utilised a small amount of vacuum grease due to low sample size. This regeneration cycle was repeated three times to assess the stability and reusability of the biochar in multi-metal adsorption systems.

## 2.2. Adsorption modelling

### 2.2.1. Isotherm models

Adsorption isotherm models describe the relationship between the concentration of adsorbate in the liquid phase and the amount adsorbed onto the solid phase, providing valuable insights into the adsorption capacity of a material. These models are essential for understanding the mechanisms of adsorption and the interactions between adsorbates and adsorbents. By analysing adsorption isotherms, the efficiency of adsorbents in removing heavy metals from aqueous solutions can be evaluated. Herein, four multi-component adsorption isotherm models were used to fit the experimental equilibrium data, namely Extended Langmuir (EL) [28], Extended Langmuir–Freundlich (LF) [29], Modified Competitive Langmuir (MCL) [30], and Extended Sips (ES) [31], as provided in Eqs. (1) to (4):

$$\text{EL model : } q_{e,i} = q_{m,i} \frac{K_{L,i} C_{e,i}}{1 + \sum_{j=1}^N K_{L,j} C_{e,j}} \quad (1)$$

$$\text{LF model : } q_{e,i} = q_{m,i} \frac{K_{LF,i} C_{e,i}^{\frac{1}{n_i}}}{\sum_{j=1}^N K_{LF,j} C_{e,j}^{\frac{1}{n_j}}} \quad (2)$$

$$\text{MCL model : } q_{e,i} = q_{m,i} \frac{K_{L,i} \frac{C_{e,i}}{\eta_{L,i}}}{1 + \sum_{j=1}^N K_{L,j} \frac{C_{e,j}}{\eta_{L,j}}} \quad (3)$$

$$\text{ES model : } q_{e,i} = q_{m,i} \frac{K_{s,i} C_{e,i}^m}{\sum_{j=1}^N K_{LF,j} C_{e,j}^m} \quad (4)$$

Where  $q_{m,i}$  is the maximum adsorption capacity (mg/g),  $C_{e,i}$  is the heavy metal ion concentration at equilibrium ( $\text{mg L}^{-1}$ ),  $K$  is the isotherm constant,  $n_i$  is the Freundlich model exponent,  $\eta$  is the correction factor of the Langmuir model,  $m$  is the Sips model exponent, and  $q_{e,i}$  is the amount of metal ions adsorbed at equilibrium per mass unit of adsorbent as given by Eq. (5):

$$q_e = \frac{(C_i - C_e) V}{M} \quad (5)$$

Where  $C_i$  is the initial concentration of metal ion ( $\text{mg L}^{-1}$ ),  $V$  is the solution volume (L), and  $M$  is the mass of the adsorbent (g). For each model, the parameters and constants were determined using the “solver add-in” in Microsoft Excel, aiming to maximise the average correlation coefficients  $R^2$  of all metal ions. The solver uses the Generalized Reduced Gradient (GRG) Nonlinear engine for smooth nonlinear correlations with a convergence of 0.0001 and a population size of 100.

### 2.2.2. Kinetics models

To understand the mechanisms of heavy metal ion adsorption into KOH-activated bagasse-derived biochar and the key factors governing sorption kinetics, experimental data were fitted to PFO and PSO models (Eqs. (6) and (7)). These models evaluated the adsorption rate and identified the dominant kinetic processes. The analysis provides insights into the rate-controlling steps and adsorption mechanism.

$$\text{PFO : } q_t = q_e (1 - e^{-k_1 t}) \quad (6)$$

$$\text{PSO : } q_t = \frac{q_e^2 k_2 t}{1 + k_2 q_e t} \quad (7)$$

Where  $q_t$  and  $q_e$  are the adsorption capacity, time =  $t$  and time =  $\infty$  (mg/g), respectively, and  $k_1$  and  $k_2$  are the adsorption rate constants of the first ( $\text{min}^{-1}$ ) and the second-order kinetic models ( $\text{mg/g}^{-1} \cdot \text{min}^{-1}$ ), respectively.

### 2.2.3. Adsorption thermodynamics

Determining the enthalpy, entropy, and Gibbs free energy of heavy metal adsorption facilitates the understanding of thermodynamic

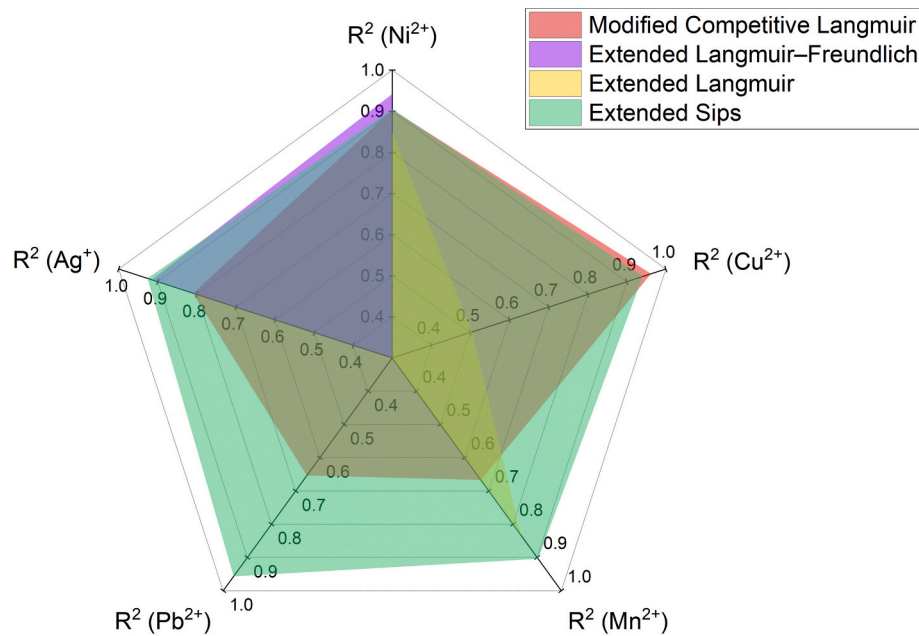


Fig. 2. The average correlation coefficients  $R^2$  of all metal ions data fitting from different isotherm models.

feasibility of the process. Enthalpy reveals whether the process is exothermic or endothermic, while entropy indicates changes in disorder. Gibbs free energy determines whether adsorption is spontaneous, providing crucial insights into the practical viability of the process for applications like water treatment. The change in enthalpy ( $\Delta H$ ) and entropy ( $\Delta S$ ) were determined by the linear regression of the Van't Hoff equation (Eq. (8)):

$$\ln(K_c) = -\frac{\Delta H}{R} \frac{1}{T} + \frac{\Delta S}{R} \quad (8)$$

Where  $R$  is the gas constant ( $8.314 \text{ J} \cdot \text{mol}^{-1} \text{ K}^{-1}$ ),  $T$  is the temperature (K), and  $K_c$  is the adsorption equilibrium constant, which is defined as the ratio of the activity of the adsorbed ions on the biochar to its activity in the liquid phase at equilibrium.  $\ln(K_c)$  was determined as an intercept by plotting  $\ln(q_e/C_e)$  against  $C_e$  and extrapolating the data to  $C_e = 0$  [32]. Lastly, the free energy change ( $\Delta G$ ) was determined from Eq. (9).

$$\Delta G = \Delta H - T\Delta S \quad (9)$$

The activation energy ( $E_a$ ) and the pre-exponential factor ( $A$ ) of the chemisorption was estimated by the linear fitting of the Arrhenius equation (Eq. (10)), where  $\ln(k)$  was plotted against  $\frac{1}{T}$  for each metal.

The values of  $E_a$  and  $A$  were obtained from the gradient and the y-intercept, respectively.

$$\ln(k) = -\frac{E_a}{R} \left(\frac{1}{T}\right) + \ln(A) \quad (10)$$

Where  $k$  is the adsorption rate constant obtained from PSO model.

### 3. Results and discussion

#### 3.1. Equilibrium studies

Fitting the experimental data using competitive adsorption isotherm models revealed that the ES isotherm model provided the best fit, with an average  $R^2$  value of 0.93, followed by the MCL model, with an average  $R^2$  of 0.80. Fig. 2 compares the  $R^2$  values for data fitting of each heavy metal ion across all models. While some models showed high  $R^2$  values for certain metals, others did not perform as well. The EF model incorporates elements from both the Langmuir and Freundlich models. It is particularly useful for describing adsorption processes in systems where adsorption behaviour deviates from the ideal Langmuir isotherm, particularly on heterogeneous surfaces with sites of varying affinities. A

Table 2  
The parameters of competitive adsorption isotherm models.

Model	Parameters	Heavy metal ions				
		$Ni^{2+}$	$Cu^{2+}$	$Mn^{2+}$	$Pb^{2+}$	$Ag^+$
ES	$q_{m,i}$ (mg/g)	494.0	501.8	414.0	605.6	468.9
	$K_s$	0.002	0.026	0.015	0.027	0.012
	$m$	1.00	0.68	0.45	1.00	0.96
	$R^2$	0.91	0.94	0.90	0.96	0.93
MCL	$q_{m,i}$ (mg/g)	6886.1	985.2	9027.6	14,277.4	9686.0
	$K_L$	0.049	0.233	0.035	1.127	0.042
	$\eta$ (mg L <sup>-1</sup> )	5.07	1.82	7.32	73.29	4.24
	$R^2$	0.90	0.96	0.67	0.65	0.81
LF	$q_{m,i}$ (mg/g)	157,198.5	22,268.0	511,960.0	37,616.0	47,346.6
	$K_{LF}$	0.00001	0.01251	0.00020	0.00501	0.00130
	$n$	1.74	352,410.17	2.76	333,803.43	1.24
	$R^2$	0.94	0.00	0.88	0.00	0.92
EL	$q_{m,i}$ (mg/g)	1,679,726.5	421,404.2	3,754,213.2	6623.7	151.1
	$K_L$	1.11	7.47	0.32	697.38	13,313.58
	$R^2$	0.85	0.50	0.83	0.00	0.00

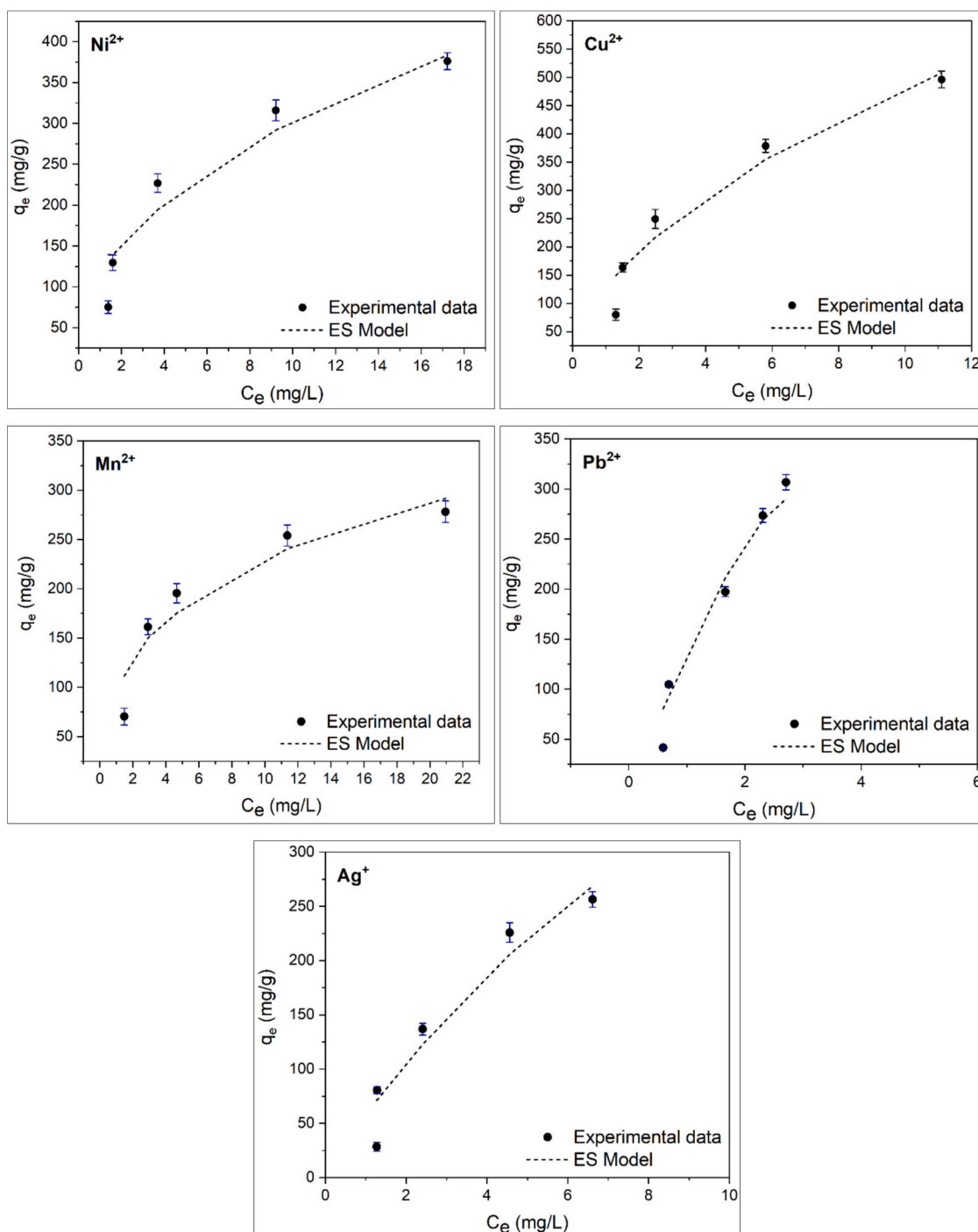


Fig. 3. The adsorption isotherms of the heavy metals based on experimental data and ES model.

high value of the coefficient  $m$  in Eq. (4) indicates that the adsorption process follows the Langmuir isotherm, while lower values of  $m$  suggest that the adsorption of heavy metals follow the Freundlich isotherm [33].

Table 2 presents the results of the isotherm model fitting for all models. The adsorbed concentrations of heavy metals based on the experimental data and the ES model are shown in Fig. 3. The findings indicate that  $Pb^{2+}$  has the highest adsorption capacity at 605.45 mg/g, followed by  $Cu^{2+}$  with 501.77 mg/g. The excellent adsorption performance of  $Pb^{2+}$  can be attributed to its relatively large ionic radius ( $\sim 133$  pm as a 6-coordinate, octahedral ion) and high electronegativity (2.33). The larger size of  $Pb^{2+}$  allows it to block pores, preventing the adsorption of other ions, while its high electronegativity enhances its

affinity for active sites on the biochar surface.

In contrast  $Cu^{2+}$ , which has a smaller ionic radius ( $\sim 87$  pm as a 6-coordinate, octahedral ion), exhibits a high electronegativity (2.0), contributing to its strong adsorption. Although  $Ag^+$  is larger than  $Cu^{2+}$  ( $\sim 108$  pm as a 6-coordinate, octahedral ion), its monovalent nature limits its ability to form bonds with the active sites on the biochar surface.  $Mn^{2+}$  demonstrates the lowest adsorption performance, with 414.02 mg/g, primarily due to its lower electronegativity (1.55). Metal ions with higher electronegativity interact more easily with the negatively charged oxygen in hydroxyl groups on the biochar surface [34]. Moreover, the adsorption of smaller ions with moderate electronegativity, such as  $Mn^{2+}$  and  $Ni^{2+}$ , can be inhibited by larger ions with higher

**Table 3**  
The kinetic parameters of PFO and PSO models.

Temperature (°C)	Model	Parameters	Heavy metal ions				
			Ni <sup>2+</sup>	Cu <sup>2+</sup>	Mn <sup>2+</sup>	Pb <sup>2+</sup>	Ag <sup>+</sup>
25	PFO	$q_e$ (mg/g)	231.8	249.6	196.4	196.5	137.3
		$k_1$ (min <sup>-1</sup> )	0.9066	0.9040	0.8273	0.9537	0.7783
		R <sup>2</sup>	0.93	0.98	0.95	0.89	0.88
	PSO	$q_e$ (mg/g)	234.3	257.3	204.7	204.9	148.5
		$k_2$ (mg/g min <sup>-1</sup> )	0.0078	0.0071	0.0067	0.0076	0.0061
		R <sup>2</sup>	0.99	0.99	0.99	0.97	0.92
35	PFO	$q_e$ (mg/g)	232.1	240.2	214.8	178.1	150.4
		$k_1$ (min <sup>-1</sup> )	0.8856	0.7728	0.8782	0.8904	0.7936
		R <sup>2</sup>	0.96	0.96	0.94	0.99	0.99
	PSO	$q_e$ (mg/g)	234.9	245.7	220.6	182.8	154.4
		$k_2$ (mg/g min <sup>-1</sup> )	0.0095	0.0074	0.0085	0.0166	0.0153
		R <sup>2</sup>	0.99	0.99	0.98	0.99	0.98
45	PFO	$q_e$ (mg/g)	252.5	260.8	206.6	173.0	150.9
		$k_1$ (min <sup>-1</sup> )	0.9395	0.9201	0.9376	0.9669	0.8829
		R <sup>2</sup>	0.97	0.97	0.97	0.95	0.89
	PSO	$q_e$ (mg/g)	262.5	273.9	209.9	177.0	148.5
		$k_2$ (mg/g min <sup>-1</sup> )	0.0115	0.0088	0.0120	0.0267	0.0155
		R <sup>2</sup>	0.98	0.99	0.99	0.99	0.98
55	PFO	$q_e$ (mg/g)	252.7	253.1	189.7	165.5	156.7
		$k_1$ (min <sup>-1</sup> )	0.9233	0.8915	0.9845	0.9376	0.9096
		R <sup>2</sup>	0.91	0.96	0.89	0.93	0.99
	PSO	$q_e$ (mg/g)	249.8	264.1	206.2	168.8	165.5
		$k_2$ (mg/g min <sup>-1</sup> )	0.0145	0.0109	0.0117	0.0299	0.0149
		R <sup>2</sup>	0.99	0.99	0.96	0.99	0.96

charge densities, such as Pb<sup>2+</sup>. The larger ions can block the pores and form stronger bonds with -OH sites on the biochar, reducing the available surface area for the adsorption of smaller ions. Kong, et al. [35] found that the adsorption capacity of heavy metals positively correlates with ionic radius. The adsorption behaviour indicates antagonistic interactions, where dominant ions like Pb<sup>2+</sup> and Cu<sup>2+</sup> outcompete others such as Mn<sup>2+</sup>, Ag<sup>+</sup> and Ni<sup>2+</sup> for active sites, reducing their uptake. Except Cu<sup>2+</sup>, it is difficult to compare the competitive adsorption capacity to their single-component case due to data unavailability using the same adsorbent. For Cu<sup>2+</sup>, the equilibrium adsorption capacity is lower than that of the signal-ion adsorption, with 389.8 mg/g in the present study and 257.3 mg/g in Bongosia, et al. [18], respectively. This is likely due to an antagonistic interaction between the ions during the multi-component adsorption. Overall, the adsorption capacity of the biochar followed the order Pb<sup>2+</sup> > Cu<sup>2+</sup> > Ni<sup>2+</sup> > Ag<sup>+</sup> > Mn<sup>2+</sup>, demonstrating strong ion adsorption selectivity.

Fitting the adsorption data of five adsorbates simultaneously using multi-component isotherm models is a challenging task, requiring longer computational times due to the numerous parameters involved. Most studies typically apply multi-component isotherm models to binary systems [25], where the complexity is lower and fewer interactions between adsorbates need to be considered. The increase in the number of components introduces additional complexities, such as competitive adsorption and site heterogeneity, making it difficult to obtain accurate and reliable model fits. For Pb<sup>2+</sup> and Ag<sup>+</sup> in the EL and LF models (Table 2), an R<sup>2</sup> value of zero indicates that the model's assumptions or structure fail to adequately describe the experimental data for these ions. This could be due to the complex interactions among the competing ions, which the models may not be able to capture, or other factors specific to these metals which are not accounted for in the models might influence the adsorption process [36].

### 3.2. Kinetics studies

The kinetics of the heavy metal adsorption on biochar were investigated using PFO and PSO models at 25 °C, 35 °C, 45 °C and 55 °C. Table 3 displays the kinetic parameters for the heavy metals at different temperatures. The experimental and predicted adsorption capacity of each metal as a function of contact time at 25 °C are shown in Fig. 4. The

results showed that the PSO model is clearly a better fit for the experimental data, especially for Cu<sup>2+</sup>, Mn<sup>2+</sup> and Pb<sup>2+</sup> ions, where the R<sup>2</sup> values are consistently >0.98. This suggests chemisorption or strong ion-adsorbent interactions [37,38]. For Ag<sup>+</sup>, while the PSO model fits better than the PFO model, the overall R<sup>2</sup> values are lower, indicating that the adsorption of Ag<sup>+</sup> may involve more complex mechanisms or weaker interactions (van der Waals) with the adsorbent [39].

Generally, the rate constant of the PFO model is higher than that of the PSO, indicating faster but weaker physical interactions compared to the chemical equivalents [40]. The temperature increase enhances both the adsorption capacity and the rate constant, particularly for Pb<sup>2+</sup>, which shows the highest affinity for the adsorbent. Temperature increases the ions kinetic energy, hence the frequency of effective collisions in the mixed solution with the biochar surface which explains the increase in the rate constant [41].

In order to determine the rate-limiting step that controls the present adsorption, the multi-mechanism adsorption kinetic model was used, Eq. (11) [42]:

$$\frac{1}{\alpha + \frac{\alpha M q_e^2}{V c_0 q_m} - 2} \left\{ \left[ 1 - \alpha + \frac{\alpha M q_e}{V c_0} \left( 1 - \frac{q_e}{q_m} \right) \right] \ln \left( 1 - \frac{q}{q_e} \right) + \left( 1 - \frac{\alpha M q_e}{V c_0} \right) \ln \left[ 1 + \left( 1 - \alpha - \frac{\alpha M q_e^2}{V c_0 q_m} \right) \frac{q}{q_e} \right] \right\} = kt \quad (11)$$

Where  $c_0$  is the initial concentration of heavy metal ion,  $\alpha$  is a dimensionless parameter, and  $k$  is an apparent rate constant. The value of  $\alpha$  indicates the rate-limiting step in the adsorption process. When,  $\alpha$  value is close to zero, the adsorption is limited to intraparticle diffusion, while when  $\alpha$  value is close to 1, the film diffusion is the dominant step. If  $\alpha$  is close to 0.5, this indicates that either chemisorption or physisorption is the prevailing step in the process [42]. For each metal ion and temperature, the values of  $\alpha$  and  $k$  were estimated using the "Solver" add-in in Microsoft Excel, as displayed in Table 4.

From Table 4, at low temperatures,  $\alpha$  values are relatively low indicating that intraparticle diffusion is the limiting step for the adsorption of ions. The resistance to mass transfer inside the biochar pores controls the adsorption. As the temperature increased to 55 °C,  $\alpha$  values for ions significantly increased, making chemisorption and physisorption the dominant steps. The temperature enhances the

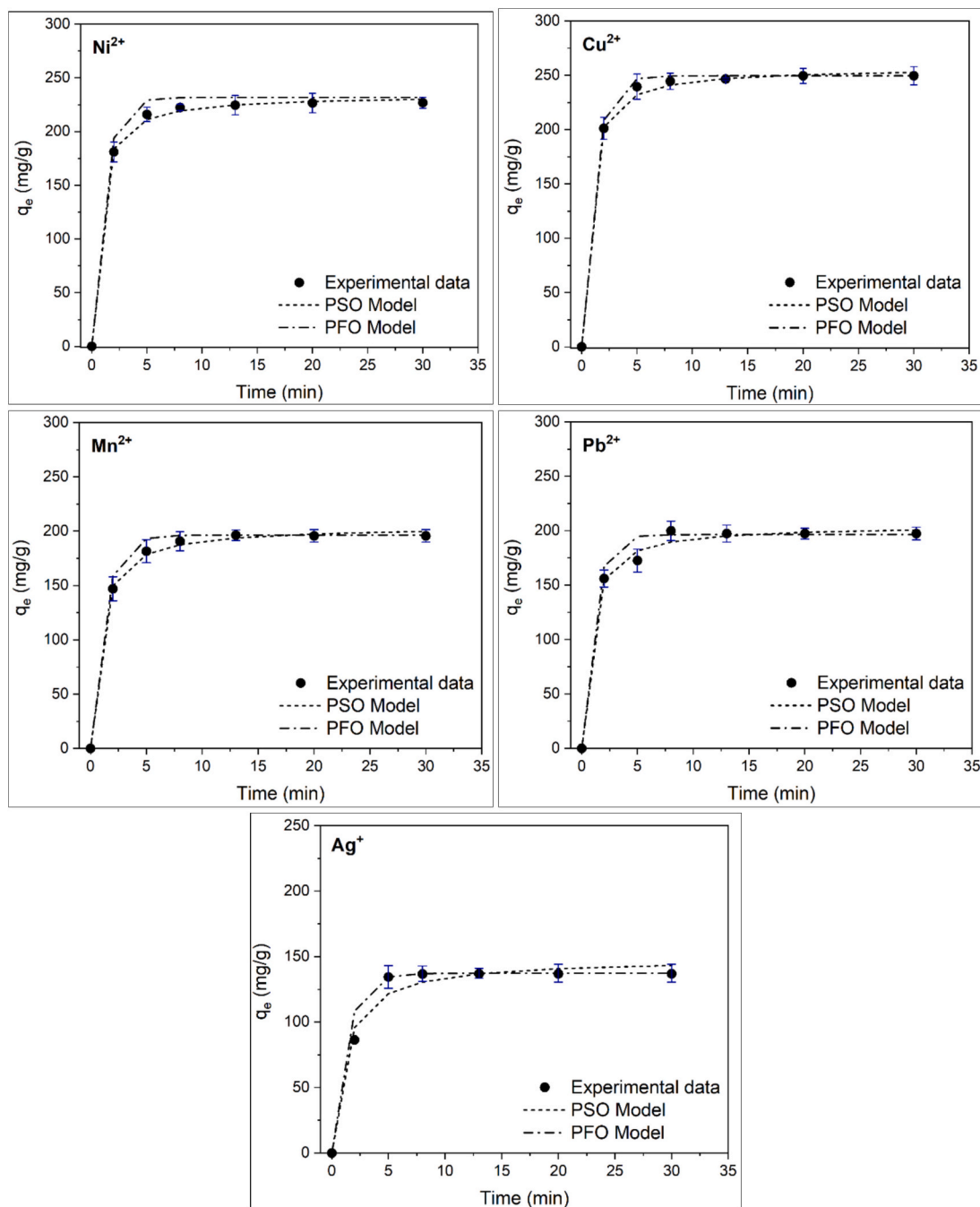


Fig. 4. The adsorption kinetics of the biochar for heavy metals based on PFO and PSO models at 25 °C.

Table 4  
The kinetic parameters of multi-mechanism adsorption kinetic model.

Temperature (°C)	Parameters	Heavy metal ions				
		Ni <sup>2+</sup>	Cu <sup>2+</sup>	Mn <sup>2+</sup>	Pb <sup>2+</sup>	Ag <sup>+</sup>
25	$\alpha$	0.1659	0.1471	0.1178	0.0824	0.0521
	$k$ (min <sup>-1</sup> )	0.1830	0.2859	0.2699	0.3506	0.3644
35	$\alpha$	0.2580	0.2648	0.2956	0.3164	0.2456
	$k$ (min <sup>-1</sup> )	0.1765	0.1498	0.2656	0.2438	0.2922
45	$\alpha$	0.5495	0.5591	0.4895	0.5451	0.4116
	$k$ (min <sup>-1</sup> )	0.2052	0.3245	0.2022	0.1821	0.2192
55	$\alpha$	0.5710	0.5946	0.5142	0.5952	0.5005
	$k$ (min <sup>-1</sup> )	0.1499	0.1751	0.1679	0.1790	0.2507

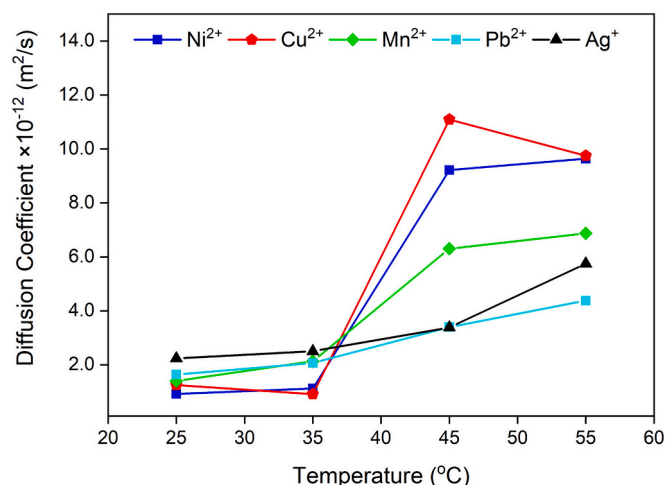


Fig. 5. The effect of temperature on the intraparticle diffusion coefficient.

intraparticle diffusion due to the increased kinetic energy of ions transporting through the pores, hence the increase in the diffusion coefficient [43], as shown in Fig. 5. Overall, the film diffusion is negligible in all temperatures due to the agitation of the solution, which increases the flow turbulence and reduces the boundary layer around the adsorbent particles [44]. To prove the positive impact of temperature on the intraparticle diffusion, the intraparticle diffusion coefficient ( $D_i$ ) was determined using the following correlation (Eq. (12)):

$$D_i = \frac{kR^2}{\pi^2 \left[ \frac{1 - \alpha + \frac{amq_e}{Vc_0} \left( 1 - \frac{q_e}{qm} \right)}{2 - \alpha - \frac{amq_e^2}{Vc_0^2 qm}} \left( 1 + \frac{mq_e}{V} \right) - \frac{amq_e}{V} \right]} \quad (12)$$

Where  $R$  is the biochar particle radius. For the KOH-activated bagasse-derived biochar,  $R$  was averaged at 114  $\mu\text{m}$  from SEM images using Fiji (ImageJ)2 software (V 1.54 m). The effect of temperature on the intraparticle diffusion coefficient is shown in Fig. 5. The results indicate that the intraparticle diffusion coefficient increases with temperature, which is attributed to the enhanced kinetic energy of the ions [45]. This increase in the intraparticle diffusion coefficient suggests a reduction in resistance to the transport of ions within the pores of the biochar. However, the influence of temperature on the diffusion coefficient diminishes at higher temperatures. Clearly, the diffusion coefficients of smaller and lighter ions, such as  $\text{Ni}^{2+}$ ,  $\text{Cu}^{2+}$ , and  $\text{Mn}^{2+}$ , are higher than those of larger and heavier ions like  $\text{Ag}^+$  and  $\text{Pb}^{2+}$ , particularly at elevated temperatures. Fig. 6 illustrates the proposed external and

internal diffusion of the metals in the biochar mesoporous network, interacting with the carbons and surface hydroxyls.

### 3.3. Adsorption thermodynamics studies

The thermodynamic study reveals the role of temperature for adsorption and to verify whether adsorption occurs spontaneously in adsorption processes. The changes in enthalpy and entropy were determined by fitting the experimental data according to Eq. (8), as shown in Fig. 7. The thermodynamic adsorption parameters and the Arrhenius constants are presented in Table 5. The positive enthalpies of adsorption for all metals indicate that the process is endothermic, becoming more thermodynamically favourable at higher temperatures.

The high  $\Delta H$  of  $\text{Pb}^{2+}$ ,  $\text{Cu}^{2+}$  and  $\text{Ni}^{2+}$  indicates stronger, more energetically demanding interactions between the metal ion and the adsorbent [46,47].  $\text{Pb}^{2+}$  has a large ionic radius coupled with high electronegativity, enabling it to form the strongest binding interactions. In contrast,  $\text{Cu}^{2+}$  and  $\text{Ni}^{2+}$  despite their smaller ionic size, exhibit higher electronegativity compared to  $\text{Mn}^{2+}$  and  $\text{Ag}^+$ . Metal ions with greater electronegativity more easily interact with the negatively charged oxygen in hydroxyl functional groups, enhancing their adsorption affinity [34].

The positive entropy changes suggest that the adsorption of heavy metals onto biochar is a spontaneous process under the given conditions. The spontaneity of the process is further confirmed by the negative values of Gibbs free energy, which decrease as temperature increases. This indicates that higher temperatures accelerate the adsorption process. These thermodynamic parameters provide key insights that influence the practical design and optimization of heavy metal adsorption processes. KOH-activated bagasse-derived biochar spontaneously removes the  $\text{Pb}^{2+}$ ,  $\text{Cu}^{2+}$  and  $\text{Ni}^{2+}$ , the metals with known toxicological profiles and health impacts, from an aqueous solution. Moreover, the adsorption rate increases with temperature due to the endothermic nature of the process.

Regarding the kinetics parameters, the  $E_a$  values range from 11.68 to 37.74 kJ/mol, suggesting that the adsorption processes are predominantly physical to moderately chemical.  $\text{Pb}^{2+}$  exhibited the highest  $E_a$  (37.74 kJ/mol), indicating a stronger interaction and higher energy barrier for adsorption, consistent with its highest adsorption capacity and preference for chemisorption. However,  $\text{Pb}^{2+}$  has a significantly high  $A$  value (35,810.4  $\text{mg/g min}^{-1}$ ), supporting its strong affinity and frequent interaction with the adsorbent surface. In contrast,  $\text{Cu}^{2+}$  showed the lowest  $E_a$  (11.68 kJ/mol), suggesting faster and more energetically accessible adsorption.

### 3.4. Stability of biochar after regeneration

The structural stability of the biochar after repeated

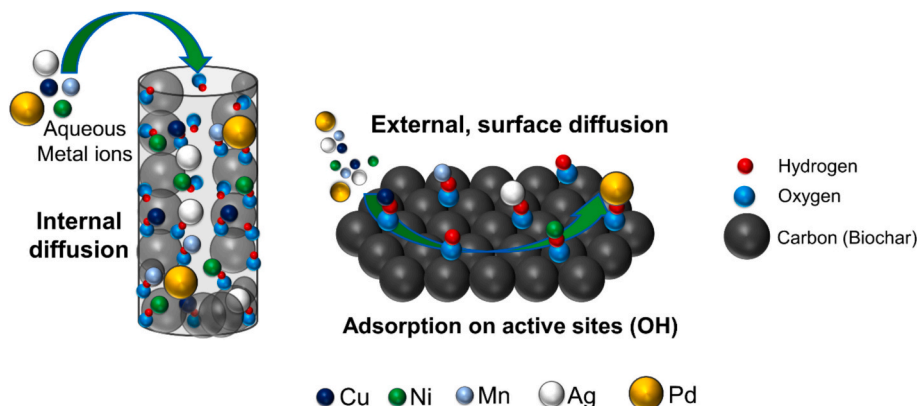
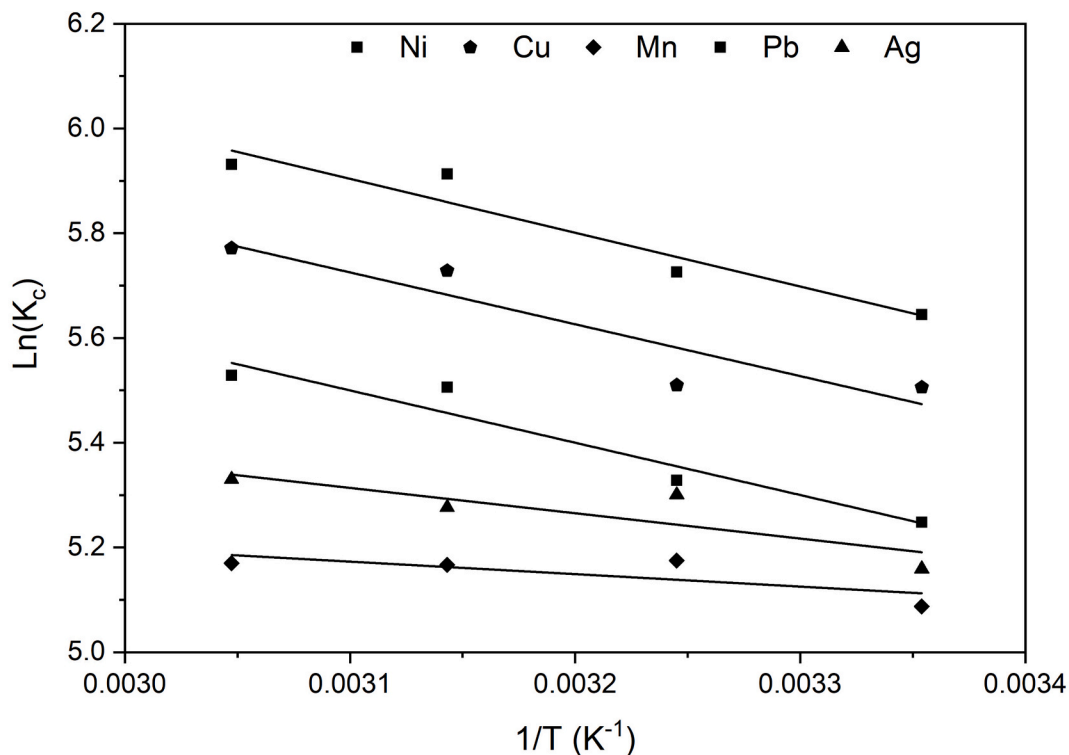


Fig. 6. The external and internal diffusion of the heavy metals in the biochar structure.



Plot	Ni	Cu	Mn	Pb	Ag
Intercept	8.596 ± 0.601	8.794 ± 0.900	5.912 ± 0.468	9.091 ± 0.658	6.813 ± 0.672
Slope	-998.6 ± 188.0	-990.0 ± 281.2	-238.4 ± 146.2	-1028.1 ± 205.7	-483.7 ± 210.0
R-Square (COD)	0.934	0.861	0.571	0.926	0.726

Fig. 7. Linear fitting curves of Eq. (8) for thermodynamic parameter determination.

Table 5

The thermodynamic parameters and the Arrhenius constants of heavy metals adsorption.

Parameter	Heavy metal ions				
	Ni <sup>2+</sup>	Cu <sup>2+</sup>	Mn <sup>2+</sup>	Pb <sup>2+</sup>	Ag <sup>+</sup>
$\Delta H$ (kJ/mol)	8.30	8.23	1.98	8.55	4.02
$\Delta S$ (J mol <sup>-1</sup> K <sup>-1</sup> )	71.46	73.11	49.15	75.58	56.65
$E_a$ (kJ/mol)	16.57	11.68	16.74	37.74	22.40
$A$ (mg/g min <sup>-1</sup> )	6.1	66.7	5.9	35,810.4	0.7

Temperature (°C)	$\Delta G$ (kJ/mol)				
25	-13.00	-13.57	-12.67	-13.99	-12.87
35	-13.72	-14.30	-13.16	-14.74	-13.43
45	-14.43	-15.03	-13.66	-15.50	-14.00
55	-15.15	-15.76	-14.15	-16.25	-14.57

adsorption-desorption cycles was evaluated using XRD analysis, as shown in Fig. 8. The diffractograms for Cycle 1, Cycle 2, and Cycle 3 reveal consistent structural features, indicating that the biochar maintains its framework after multiple regeneration steps.

Three key peaks are observed in the XRD spectra. Peak 1, at ~16°, is attributed to residual grease used during the sample preparation process, as previously reported by our group [27]. Peak 2, located at ~25°, corresponds to the characteristic broad signal of amorphous carbon, which is typical for biochar and reflects its disordered structure. Peak 3, appearing ~42°, represents the presence of turbostratic carbon, a form

of structurally disordered graphite-like carbon.

Importantly, the intensity and positions of Peaks 2 and 3 remain largely unchanged over the three cycles, suggesting that the carbon structure of the biochar is resilient to acidic regeneration using 5 M HCl. No new crystalline phases or metal products are observed, confirming the chemical and structural stability of the biochar during reuse.

#### 4. Conclusions

In this work, the modelling of the adsorption of five heavy metals (Cu, Ni, Pb, Ag and Mn) in mesoporous sugarcane bagasse-derived biochar was carried out. For the adsorption isotherms, multi-component models namely EL, EF, MCL and ES were employed. The multi-component models showed better performance in describing competitive adsorption and capturing multi-ion interactions. The ES isotherm model provided the best fit for the experimental data, with an average R<sup>2</sup> value of 0.93. The findings also indicate that Pb<sup>2+</sup> has the highest adsorption capacity at 605.45 mg/g, followed by Cu<sup>2+</sup> with 501.77 mg/g. The ion selectivity of the biochar follows the order of Pb<sup>2+</sup> > Cu<sup>2+</sup> > Ni<sup>2+</sup> > Ag<sup>+</sup> > Mn<sup>2+</sup>. Regarding the adsorption kinetics, the experimental data were fitted to PFO and PSO models. The PSO model is a better fit for the experimental data, especially for Cu<sup>2+</sup>, Mn<sup>2+</sup>, and Pb<sup>2+</sup> ions, suggesting chemisorption or strong ion-adsorbent interactions.

The rate-limiting step that controls the adsorption process was determined by adopting a recently proposed multi-mechanism kinetic model. At low temperatures, intraparticle diffusion is the limiting step

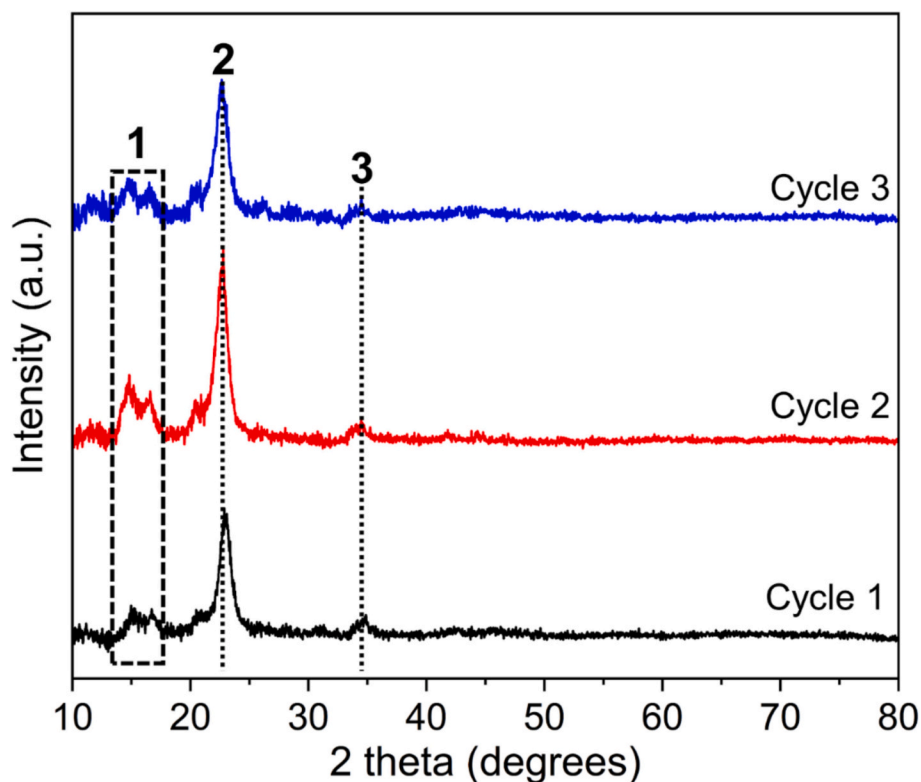


Fig. 8. The XRD patterns of the biochar at different adsorption-desorption cycles.

for adsorption of ions, while chemisorption and physisorption became dominant at higher temperatures. The intraparticle diffusion coefficient increased with temperature. Finally, the thermodynamic parameters of the multi-component adsorption process were determined. The positive enthalpies for all metals indicate that the process is endothermic, while the positive entropy changes and negative Gibbs free energies suggest that a spontaneous adsorption of heavy metals under the optimum conditions. The XRD results demonstrated that the biochar maintained its amorphous and turbostratic carbon structure over three regeneration cycles, indicating high structural resilience and reusability. Overall, this study is combining an affordable, scalable, waste-derived material with detailed modelling to better explain how and why some metals are removed more than others.

#### CRediT authorship contribution statement

**Amthal Al-Gailani:** Writing – original draft, Methodology, Investigation, Funding acquisition, Formal analysis, Data curation, Conceptualization. **Julius G. Bongosia:** Writing – original draft, Methodology, Investigation. **Karl Hornsby:** Investigation, Methodology. **Martin J. Taylor:** Writing – review & editing, Project administration, Methodology.

#### Declaration of competing interest

The authors declare that they have no known competing financial interests or personal relationships that could have appeared to influence the work reported in this paper.

#### Acknowledgement

The authors acknowledge the funding and support from the Higher Education Innovation Funding (HEIF) program at the University of Hull.

#### Data availability

Data will be made available on request.

#### References

- [1] Q. Zhou, N. Yang, Y. Li, B. Ren, X. Ding, H. Bian, X. Yao, Total concentrations and sources of heavy metal pollution in global river and lake water bodies from 1972 to 2017, *Glob. Ecol. Conserv.* 22 (2020) e00925, <https://doi.org/10.1016/j.gecco.2020.e00925>.
- [2] S. Mitra, A.J. Chakraborty, A.M. Tareq, T.B. Emran, F. Nainu, A. Khusro, A.M. Idris, M.U. Khandaker, H. Osman, F.A. Alhumaydhi, J. Simal-Gandara, Impact of heavy metals on the environment and human health: novel therapeutic insights to counter the toxicity, *J. King Saud Univ. - Sci.* 34 (3) (2022) 101865. Art no. <https://doi.org/10.1016/j.jksus.2022.101865>.
- [3] EPA, "Potential Well Water Contaminants and Their Impacts." United States Environmental Protection Agency. <https://www.epa.gov/privatewells/potential-well-water-contaminants-and-their-impacts>, 2024 (accessed Feb 14, 2025).
- [4] Y. Zhang, B. Jiang, Z. Gao, M. Wang, J. Feng, L. Xia, J. Liu, Health risk assessment of soil heavy metals in a typical mining town in north China based on Monte Carlo simulation coupled with Positive matrix factorization model, *Environ. Res.* 251 (2024) 118696. Art no. <https://doi.org/10.1016/j.envres.2024.118696>.
- [5] I. f. H. M. a. Evaluation., Lead exposure-Level 3 risk, University of Washington, Seattle, 2024. <https://www.healthdata.org/research-analysis/diseases-injuries-risks/factsheets/2021-lead-exposure-level-3-risk> (accessed).
- [6] I. f. H. M. a. Evaluation., Occupational Exposure to Nickel - Level 4 Risk, University of Washington, Seattle, 2024. <https://www.healthdata.org/research-analysis/diseases-injuries-risks/factsheets/2021-occupational-exposure-nickel-level-4-risk> (accessed).
- [7] M. Dave, A. Busby, L.A. Shammari, N. Iqbal, L. Coole, H. Bagnall, H. Crabbe, Lead exposure sources and public health investigations for children with elevated blood lead in England, 2014 to 2022, *PLoS One* 19 (7) (2024) e0304866, <https://doi.org/10.1371/journal.pone.0304866>.
- [8] N.D. Nnaji, H. Onyeaka, T. Miri, C. Ugwa, Bioaccumulation for heavy metal removal: a review, *SN Appl. Sci.* 5 (5) (2023) 125, <https://doi.org/10.1007/s42452-023-05351-6>.
- [9] C.P. Baldé, R. Kuehr, T. Yamamoto, R. McDonald, E. D'Angelo, S. Althaf, G. Bel, O. Deubzer, E. Fernandez-Cubillo, V. Forti, *Global e-waste monitor 2024*, International Telecommunication Union (ITU) and United Nations Institute for ... , 2024.
- [10] L. Andeobu, S. Wibowo, S. Grandhi, An assessment of e-waste generation and environmental management of selected countries in Africa, Europe and North America: a systematic review, *Sci. Total Environ.* 792 (2021) 148078. Art no. <https://doi.org/10.1016/j.scitotenv.2021.148078>.

- [11] S.C. Chakraborty, M. Qamruzzaman, M.W.U. Zaman, M.M. Alam, M.D. Hossain, B. K. Pramanik, L.N. Nguyen, L.D. Nghiem, M.F. Ahmed, J.L. Zhou, Md.Ibrahim. H. Mondal, M.A. Hossain, M.A.H. Johir, M.B. Ahmed, J.A. Sithi, M. Zargar, Mohammad Ali Moni, Metals in e-waste: occurrence, fate, impacts and remediation technologies, *Process. Saf. Environ. Prot.* 162 (2022) 230–252, <https://doi.org/10.1016/j.psep.2022.04.011>.
- [12] L. Ankit, V. Saha, J. Kumar, Sweta Tiwari, S. Rawat, J. Singh, K. Baudhdh, Electronic waste and their leachates impact on human health and environment: global ecological threat and management, *Environ. Technol. Innov.* 24 (2021) 102049. Art no. <https://doi.org/10.1016/j.eti.2021.102049>.
- [13] D. Komilis, V. Tatakis, T. Tsakmakis, Leaching of heavy metals from personal computer components: comparison of TCLP with a European leaching test, *J. Environ. Eng.* 139 (11) (2013) 1375–1381. Art no. [https://doi.org/10.1061/\(ASCE\)JEE.1943-7870.0000752](https://doi.org/10.1061/(ASCE)JEE.1943-7870.0000752).
- [14] M.R. Awual, New Type Mesoporous Conjugate Material for Selective Optical Copper(II) Ions Monitoring & Removal from Polluted Waters, *Chemical Engineering Journal* vol. 307, 2017, pp. 85–94. Art no. <https://doi.org/10.1016/j.cej.2016.07.110>.
- [15] M.R. Awual, Mesoporous composite material for efficient lead(II) detection and removal from aqueous media, *J. Environ. Chem. Eng.* 7 (3) (2019) 103124. Art no. <https://doi.org/10.1016/j.jece.2019.103124>.
- [16] F. Huang, L.-Y. Gao, R.-R. Wu, H. Wang, R.-B. Xiao, Qualitative and quantitative characterization of adsorption mechanisms for Cd<sup>2+</sup> by silicon-rich biochar, *Sci. Total Environ.* 731 (2020) 139163. Art no. <https://doi.org/10.1016/j.scitotenv.2020.139163>.
- [17] E. Liang, L. Xu, J. Su, Y. Yang, Y. Liu, Nano iron tetroxide-modified rice husk biochar promoted Feamox performance of Klebsiella sp. FC61 and synergistically removed Ni<sup>2+</sup> and ciprofloxacin, *Bioresour. Technol.* 382 (2023) 129183. Art no. <https://doi.org/10.1016/j.biortech.2023.129183>.
- [18] J.G. Bongosia, A. Al-Gailani, B.W. Kolosz, A. Loy Chun Minh, S.S.M. Lock, K. W. Cheah, M.J. Taylor, Scalable mesoporous biochars from bagasse waste for Cu (II) removal: process optimisation, kinetics and techno-economic analysis, *J. Environ. Manag.* 370 (2024) 122558, <https://doi.org/10.1016/j.jenvman.2024.122558>.
- [19] R.-Z. Wang, D.-L. Huang, Y.-G. Liu, C. Zhang, C. Lai, G.-M. Zeng, M. Cheng, X.-M. Gong, J. Wan, H. Luo, Investigating the adsorption behavior and the relative distribution of Cd<sup>2+</sup> sorption mechanisms on biochars with different feedstock, *Bioresour. Technol.* 261 (2018) 265–271. Art no., <https://doi.org/10.1016/j.biortech.2018.04.032>.
- [20] J. Liu, H. Jia, Z. Xu, T. Wang, M. Mei, S. Chen, J. Li, W. Zhang, An impressive pristine biochar from food waste digestate for arsenic(V) removal from water: performance, optimization, and mechanism, *Bioresour. Technol.* 387 (2023) 129586. Art no. <https://doi.org/10.1016/j.biortech.2023.129586>.
- [21] Z. Ahmad, B. Gao, A. Mosa, H. Yu, X. Yin, A. Bashir, H. Ghozeisi, S. Wang, Removal of Cu(II), Cd(II) and Pb(II) ions from aqueous solutions by biochars derived from potassium-rich biomass, *J. Clean. Prod.* 180 (2018) 437–449. Art no. <https://doi.org/10.1016/j.jclepro.2018.01.133>.
- [22] M.-E. Lee, J.H. Park, J.W. Chung, Comparison of the lead and copper adsorption capacities of plant source materials and their biochars, *J. Environ. Manag.* 236 (2019) 118–124. Art no. <https://doi.org/10.1016/j.jenvman.2019.01.100>.
- [23] J. Bayar, N. Ali, Y. Dong, U. Ahmad, M.M. Anjum, G.R. Khan, M. Zaib, A. Jalal, R. Ali, L. Ali, Biochar-based adsorption for heavy metal removal in water: a sustainable and cost-effective approach, *Environ. Geochem. Health* 46 (11) (2024) 428. Art no., <https://doi.org/10.1007/s10653-024-02214-w>.
- [24] Priyanka, I.E. Wood, A. Al-Gailani, B.W. Kolosz, K.W. Cheah, D. Vashisht, S. K. Mehta, M.J. Taylor, Cleaning up metal contamination after decades of energy production and manufacturing: reviewing the value in use of biochars for a sustainable future, *Sustainability* 16 (20) (2024) 8838. Art no. [Online]. Available: <https://www.mdpi.com/2071-1050/16/20/8838>.
- [25] G. Amrutha, C.R. Jeppu, B. Girish, K. Prabhu, K. Mayer, Multi-component adsorption isotherms: review and modeling studies, *Environ. Process.* 10 (2) (2023) 38, <https://doi.org/10.1007/s40710-023-00631-0> (Art no.).
- [26] J. Bayuo, M.J. Rwiza, M. Sillanpää, K.M. Mtei, Removal of heavy metals from binary and multi-component adsorption systems using various adsorbents – a systematic review, *RSC Adv.* 13 (19) (2023) 13052–13093, <https://doi.org/10.1039/D3RA01660A>.
- [27] D. Priyanka, A.O. Vashisht, S.K. Ibadon, M.J. Mehta, M.J. Taylor, Enhanced wastewater remediation using mesoporous activated wheat straw biochars: a dye removal perspective, *ACS Sustain. Resour. Manag.* 1 (2) (2024) 355–367. Art no. <https://doi.org/10.1021/acssusresmg.3c00109>.
- [28] V.C. Srivastava, I.D. Mall, I.M. Mishra, Removal of cadmium(II) and zinc(II) metal ions from binary aqueous solution by rice husk ash, *Colloids Surf. A Physicochem. Eng. Asp.* 312 (2) (2008) 172–184. Art no. <https://doi.org/10.1016/j.colsurfa.2007.06.048>.
- [29] C.S.D. Costa, B.G.M. Queiroz, R. Landers, M.G.C. da Silva, M.G.A. Vieira, Equilibrium study of binary mixture biosorption of Cr(III) and Zn(II) by dealginated seaweed waste: investigation of adsorption mechanisms using X-ray photoelectron spectroscopy analysis, *Environ. Sci. Pollut. Res.* 26 (28) (2019) 28470–28480. Art no., <https://doi.org/10.1007/s11356-018-2880-7>.
- [30] S. Sohn, D. Kim, Modification of Langmuir isotherm in solution systems—definition and utilization of concentration dependent factor, *Chemosphere* 58 (1) (2005) 115–123. Art no. <https://doi.org/10.1016/j.chemosphere.2004.08.091>.
- [31] S. Al-Asheh, F. Banat, R. Al-Omari, Z. Duvnjak, Predictions of binary sorption isotherms for the sorption of heavy metals by pine bark using single isotherm data, *Chemosphere* 41 (5) (2000) 659–665. Art no., [https://doi.org/10.1016/S0045-6535\(99\)00497-X](https://doi.org/10.1016/S0045-6535(99)00497-X).
- [32] H.-j. Yang, Z.-l. Zhang, L.-b. Yan, Z.-q. Chen, X. ju Lin, X. Cheng, J.-m. Zhou, D.-s. Wang, Y.-y. Lian, Modification of nanoscale polymeric adsorbent for the preparative separation and purification of tacrolimus from fermentation broth of \*Streptomyces tsukubaensis\*, *J. Chromatogr. A* 1675 (2022) 463180, <https://doi.org/10.1016/j.chroma.2022.463180>.
- [33] N. Tzabar, H.J.M. ter Brake, Adsorption isotherms and sips models of nitrogen, methane, ethane, and propane on commercial activated carbons and polyvinylidene chloride, *Adsorption* 22 (7) (2016) 901–914, <https://doi.org/10.1007/s10450-016-9794-9>.
- [34] J. Pan, B. Gao, K. Guo, Y. Gao, X. Xu, Q. Yue, Insights into selective adsorption mechanism of copper and zinc ions onto biogas residue-based adsorbent: theoretical calculation and electronegativity difference, *Sci. Total Environ.* 805 (2022) 150413. Art no. <https://doi.org/10.1016/j.scitotenv.2021.150413>.
- [35] Q. Kong, S. Preis, L. Li, P. Luo, C. Wei, Z. Li, Y. Hu, C. Wei, Relations between metal ion characteristics and adsorption performance of graphene oxide: a comprehensive experimental and theoretical study, *Sep. Purif. Technol.* 232 (2020) 115956. Art no. <https://doi.org/10.1016/j.seppur.2019.115956>.
- [36] M.D. Humphries, K. Gurney, A means to an end: validating models by fitting experimental data, *Neurocomputing* 70 (10) (2007) 1892–1896. Art no. <https://doi.org/10.1016/j.neucom.2006.10.061>.
- [37] Y. Chen, H. Shi, H. Guo, C. Ling, X. Yuan, P. Li, Hydrated titanium oxide nanoparticles supported on natural rice straw for Cu (II) removal from water, *Environ. Technol. Innov.* 20 (2020) 101143. Art no. <https://doi.org/10.1016/j.eti.2020.101143>.
- [38] A. El Hanandeh, Z. Mahdi, M.S. Intiaz, Modelling of the adsorption of Pb, Cu and Ni ions from single and multi-component aqueous solutions by date seed derived biochar: comparison of six machine learning approaches, *Environ. Res.* 192 (2021) 110338. Art no. <https://doi.org/10.1016/j.envres.2020.110338>.
- [39] X. Yang, Y. Wan, Y. Zheng, F. He, Z. Yu, J. Huang, H. Wang, Y.S. Ok, Y. Jiang, B. Gao, Surface functional groups of carbon-based adsorbents and their roles in the removal of heavy metals from aqueous solutions: a critical review, *Chem. Eng. J.* 366 (2019) 608–621. Art no. <https://doi.org/10.1016/j.cej.2019.02.119>.
- [40] Y.S. Ho, G. McKay, Pseudo-second order model for sorption processes, *Process Biochem.* 34 (5) (1999) 451–465. Art no. [https://doi.org/10.1016/S0032-9592\(98\)00112-5](https://doi.org/10.1016/S0032-9592(98)00112-5).
- [41] B. Bai, F. Bai, X. Li, Q. Nie, X. Jia, H. Wu, The remediation efficiency of heavy metal pollutants in water by industrial red mud particle waste, *Environ. Technol. Innov.* 28 (2022) 102944. Art no. <https://doi.org/10.1016/j.eti.2022.102944>.
- [42] C. Yao, C. Zhu, A new multi-mechanism adsorption kinetic model and its relation to mass transfer coefficients, *Surf. Interface Anal.* 26 (2021) 101422, <https://doi.org/10.1016/j.surfin.2021.101422>.
- [43] A.E. Ofomaja, Intraparticle diffusion process for lead(II) biosorption onto mansonia wood sawdust, *Bioresour. Technol.* 101 (15) (2010) 5868–5876. Art no. <https://doi.org/10.1016/j.biortech.2010.03.033>.
- [44] Q. Zhu, G.D. Moggridge, C. D'agostino, Adsorption of pyridine from aqueous solutions by polymeric adsorbents MN 200 and MN 500. Part 2: kinetics and diffusion analysis, *Chem. Eng. J.* 306 (2016) 1223–1233. Art no., <https://doi.org/10.1016/j.cej.2016.07.087>.
- [45] M. Qu, S. Li, J. Chen, Y. Xiao, J. Xiao, Ion transport in the EMITFSI/PVDF system at different temperatures: a molecular dynamics simulation, *ACS Omega* 7 (11) (2022) 9333–9342. Art no. <https://doi.org/10.1021/acsomega.1c06160>.
- [46] L. Sellaoui, S. Yahyaoui, S. Taamalli, Z. Srour, D. Franco, M. Schadeck Netto, et al., A study of single and quaternary adsorption of Cu<sup>2+</sup>, Co<sup>2+</sup>, Ni<sup>2+</sup> and Ag<sup>+</sup> on sludge modified by alkaline fusion, *Chem. Eng. J.* 433 (2022) 133674. Art no. <https://doi.org/10.1016/j.cej.2021.133674>.
- [47] B. Xu, Adsorption behavior of metal cations on gold nanoparticle surfaces studied by isothermal titration microcalorimetry, *J. Chin. Chem. Soc.* 57 (3A) (2010) 309–315. Art no., <https://doi.org/10.1002/jccs.201000046>.